atmosphere

MDPI

Article

Relationship between Near-Surface Winds Due to Tropical Cyclones and Infrared Brightness Temperature Obtained from Geostationary Satellite

Jiali Zhang [1], Qinglan Li [1,*], Wei Zhao [1], Joseph H. W. Lee [2], Jia Liu [3] and Shuxin Wang [3]

[1] Shenzhen Institute of Advanced Technology, Chinese Academy of Sciences, Shenzhen 518055, China; jl.zhang4@siat.ac.cn (J.Z.); wei.zhao2@siat.ac.cn (W.Z.)
[2] Macau Environmental Research Institute, Macau University of Science and Technology, Taipa, Macau, China; jhwlee@must.edu.mo
[3] Shenzhen Meteorological Bureau, Shenzhen 518040, China; azariasliu@gmail.com (J.L.); w0304101260@126.com (S.W.)
* Correspondence: ql.li@siat.ac.cn; Tel.: +86-755-8639-2382

Abstract: Based on ten-year tropical cyclones (TCs) observations from 2009 to 2018, the black body temperature (TBB, also called cloud-top brightness temperature) data obtained from the infrared channel 1 (with the wavelength of 10.30–11.30 μm) of the FY-2 satellite image, and the wind observation data at the automatic weather stations (AWSs) in Guangdong province, this study explores the relationship between the TBBs and the winds induced by TCs at AWSs. It is found that the wind speeds at AWSs cannot be obtained directly by using TBB value inversion, but the maximum potential wind gust (MPG) and the maximum potential average-wind (MPAW) at AWSs can be estimated when a TBB is known. Influenced by the terrain, the surrounding environment, and detected height, the MPG and the MPAW values of different AWSs may differ for the same TBB. The wind data from ERA5 reanalysis is also used to explore the relationship between the TBBs and the winds over grids area during the TCs' periods. Similar to the AWSs, there is a capping function between the winds over the grids and the TBBs. The reanalysis data can generally show the average wind conditions of the weather stations inside the grids, and therefore, can be used to supplement the data for the areas where there is no AWS observation available. Such a study could provide references for estimating the potential wind disasters induced by TCs in the study area.

Keywords: near-surface wind; black body temperature; maximum potential gust; maximum potential average-wind

Citation: Zhang, J.; Li, Q.; Zhao, W.; Lee, J.H.W.; Liu, J.; Wang, S. Relationship between Near-Surface Winds Due to Tropical Cyclones and Infrared Brightness Temperature Obtained from Geostationary Satellite. *Atmosphere* **2021**, *12*, 493. https://doi.org/10.3390/atmos12040493

Academic Editors: Wen Zhou, Carlos M. Carrillo and Jason C. Knievel

Received: 26 February 2021
Accepted: 7 April 2021
Published: 14 April 2021

1. Introduction

China is a country suffering heavily from tropical cyclones (TCs). There are about seven TCs making landfall on the southeast coast of China every year, causing more than 9000 casualties (more than 500 deaths) and economic losses accounting for about 0.4% of GDP [1]. Guangdong, located on the southern coast of China, is the area most affected by TCs in the country. Additionally, there are about 3.7 TCs making landfall in Guangdong every year [2]. In all the disasters brought by TCs, wind damage is extremely serious, which not only brings direct property losses but also determines the extent of storm surge and other secondary hazards [3]. Therefore, estimating the potential wind due to TCs is crucial for the safety of the local communities.

For a long time, scientists have been making efforts to explore ways to estimate the wind speeds induced by TCs. Yang et al. [4] believed that the differences in wind distribution caused by TCs in different seasons and different areas were closely related to their intensity at that time. The stronger the TCs were at the landing time, the greater were the wind speeds and the wider were the influencing ranges. Kaplan et al. [5] developed a model based on the observations in the Atlantic that the wind speed decay rate after TCs landfall was proportional to the wind speed. A correction term accounting for the distance of TC inland was included in the model. The model can be used to estimate the maximum inland penetration of hurricane force winds for a given initial storm intensity. Dong et al. [6] studied the wind distribution of TCs in Guangxi and established the wind prediction model of TCs by using stepwise regression and neural networks.

In the previous studies, most statistical analyses used ground observation data to compute the TC induced wind frequency [7], wind spatiotemporal characteristics [8,9], and temporal wind variation [10]. However, it is difficult to obtain real wind field data in areas without stations, such as mountains, oceans, deserts, and polar regions. Powell et al. [11] presented a method to estimate the maximum surface wind speeds from flight-level reconnaissance wind measurements. However, for regions where there is no aircraft reconnaissance for TCs, satellite data is an important source of information [12]. Satellite-derived cloud-top brightness temperature has good statistical relations with various meteorological elements [13,14]. The cloud-top brightness temperature can reflect the radiation emitted into space from the cloud-top and cloud-free or cloudless regions of the Earth's surface. It is commonly referred to as black body temperature (TBB) [15]. The lower is TBB, the higher the cloud-top height will be, which indirectly reflects the intensity of TC activity. The Dvorak technique [16,17], which estimates the intensity of TCs by analyzing satellite image patterns and infrared cloud-top temperatures, is widely used for estimating the maximum wind speeds associated with TCs [18]. DeMaria and Kaplan [19,20] set up the Statistical Hurricane Intensity Prediction Scheme (SHIPS), using some predictors related to TBB from GOES (Geostationary Operational Environmental Satellite) to predict the TCs' intensity over the Atlantic.

In addition to using TBB data as a predictor for TC intensity, the TBB data provided by satellites can also reflect the distribution of the wind and rain to some extent induced by TCs. Wind field estimation methods [21] based on the satellite infrared images were also developed. Knaff et al. [22] estimated TC size from infrared satellite imagery and global model analyses, and then combined TC location, motion, and intensity to estimate TC wind radii. Kossin et al. [23] introduced the new objective methods that use readily available data to estimate various aspects of the two-dimensional surface wind field structure in hurricanes. The methods correlate a variety of wind field metrics to combinations of storm intensity, storm position, storm age, and information derived from geostationary satellite infrared (IR) imagery. In recent decades, cloud motion wind inversion based on satellite data has been widely used in TC analysis, and its importance has been shown more intensely [24]. Le Marshall et al. [25] discussed the estimation of cloud motion wind in infrared and visible images with a high spatial and temporal resolution. At present, the most effective application of tracer cloud in cloud motion wind computing is the correlation matching method proposed by Leese et al. [26]. Additionally, Xu et al. [27] improved the algorithm and achieved remarkable results using satellite images to retrieve cloud motion wind.

Most of the existing methods of wind field inversion and wind speed estimation using satellite data aim to estimate sea surface wind field and wind speed over the ocean. There are few studies on extreme wind speed estimation near land surface (usually with a height of 10 m above ground) using satellite data. However, characteristics of the near land surface wind directly affect the social–economic development and human activities [28]. The spatial characteristics of the wind change due to the underlying surface features and the surrounding environment. In addition, the distribution of meteorological stations in complex terrain is generally sparse, making it difficult to provide a large number of reliable observation data over the remote complex region. Fortunately, satellite data have a high spatial and temporal resolution, and the data availability is not affected by the underlying surface, no matter how complicated the terrain is and how remote the area is from the city. Therefore, it is of great significance to use satellite data to estimate the extreme wind speed over the near land surface. In this study, the potential relationship between TBB data and near land surface wind speed is explored, which can be used as an early warning and prediction indicator of TC winds and provide a reliable reference tool for wind disaster prevention and mitigation.

2. Data

The data used in this paper were the hourly observations at more than 2000 regional automatic weather stations (AWSs) in Guangdong province from 2009 to 2018 provided by the China Meteorological Administration (CMA). Two kinds of hourly records were used: one is the 10-min average wind (average-wind), which is the maximum 10-min average wind speed observed within an hour; the other is the wind gust, which is the maximum 3-s average wind speed observed within an hour [29]. Unconditional use of the raw data from AWSs may sometimes lead to wrong conclusions. Therefore, it is necessary to examine the raw data before proceeding to the analysis. In this study, the data quality control implemented on the AWSs data mainly contains completeness and internal consistency checks [28]. A complete record means its information of the wind speed and direction (both for average-wind and gust) cannot be empty. Additionally, the rule for the internal inconsistency is identified as the wind gust speed is less than the average-wind speed for the same hour. Additionally, the qualified AWSs must have records of more than 90% of all hourly observations during the 10-yr TCs periods, so as to avoid excessive data missing at the stations. Finally, a total of 1263 AWSs are qualified in the study. The locations of these stations are illustrated in Figure 1. From the figure, the spatial distributions of the AWSs are more uniform and denser in the vicinity of the Pearl River Estuary, so the short-time extreme wind with high spatial and temporal resolution can be effectively detected.

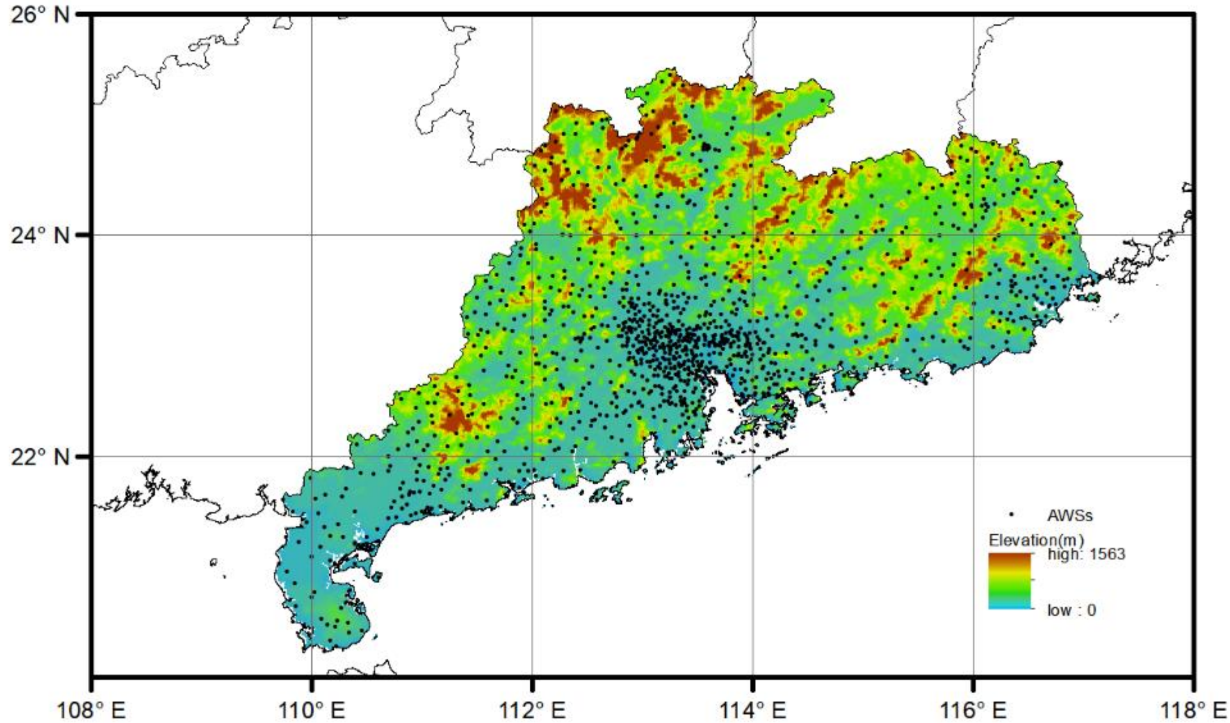

Figure 1. Locations of the automatic weather stations (AWSs) in Guangdong Province and the geographical features of the study area. The legend of the color bar exhibits the elevation of the study area.

There are 23 TCs making landfall (only considering the first landfall) along the coast of Guangdong Province from 2009 to 2018. The real-time TC track data for these 23 TCs are obtained from CMA, including the TC time (year, month, day, and hour), locations (longitude and latitude of TC center), TC intensity (sustained maximum wind speed near the center of a TC), and TC size (in terms of the radius of gale-force winds of 17 m/s).

The tracks of these 23 TCs are shown in Figure 2. The wind disaster over land due to TCs generally occurs around the TC's landfalling time [30,31]. Therefore, the hourly observations at the AWSs 12 h before and after TCs landfall were selected to explore the potential TC wind disaster. There were 551 hourly observation data available, as one of the 23 TCs only lasted 11 h after the landfall.

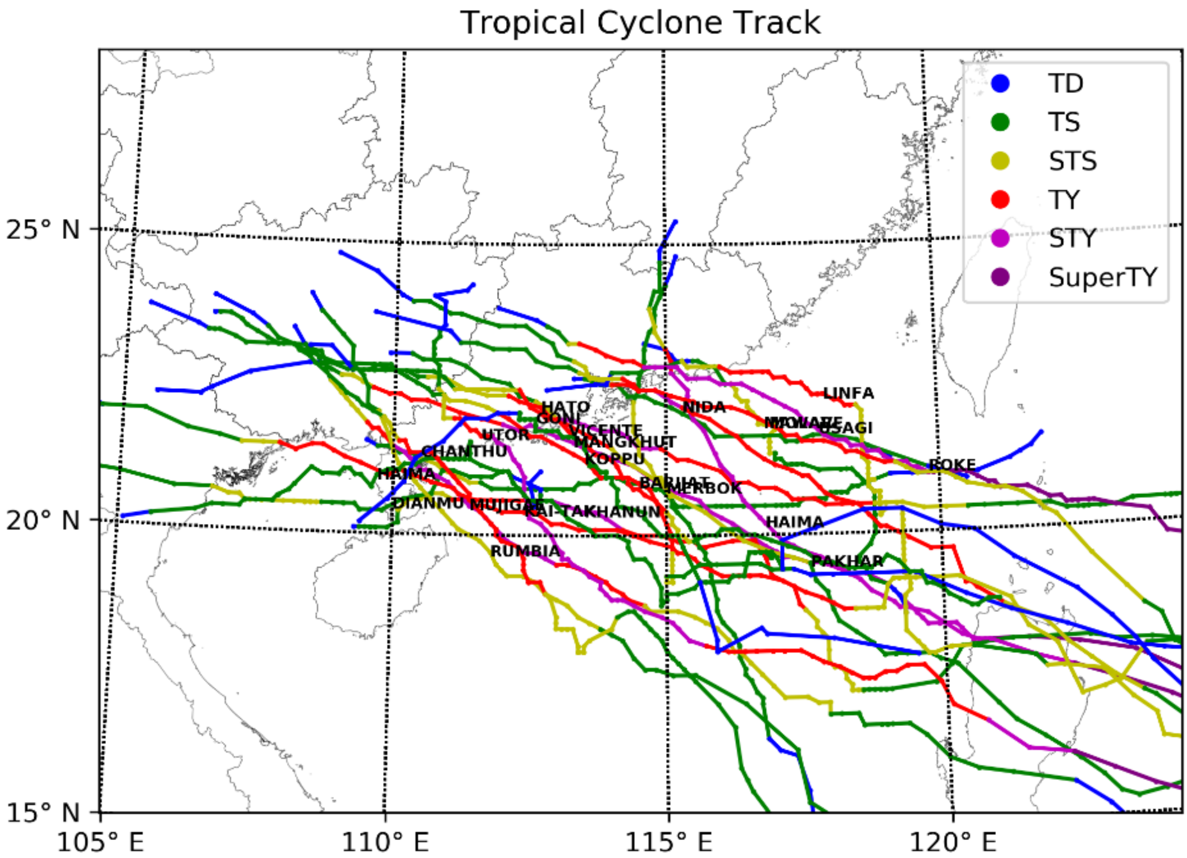

Figure 2. The tracks of 23 tropical cyclones (TCs) making landfall along the Guangdong coast from 2009 to 2018. The different colors indicate the TCs intensity.

Satellite data are obtained from the National Satellite Meteorological Center (China). The FY-2 series is the first generation of Chinese geostationary meteorological satellites, which has a frequency of half an hour for producing the cloud images [32]. In this study, we used the satellite cloud images right on every hour. These images are from FY-2D satellite for 2009, FY-2E satellite for 2010–2014, and FY-2G satellite for 2015–2018. The long-wave infrared channel (IR1, with the wavelength of 10.30–11.30 μm) has reliable detection performance. The TBB from IR1 can be guaranteed, no matter in the daytime or nighttime, and can be used for continuous monitoring. So, the TBBs obtained from the IR1 channel were used in this paper to explore the potential wind disasters. There are data missing in satellite images at some moments. A total of 526 full-disk nominal images corresponding to the 551 hourly observation data during the above TC landfalling periods are available. The spatial resolution is 5 km and the temporal resolution is an hour. To compare the difference of the satellite images between the periods with TCs and without TCs, other 4815 satellite images during June-September without TCs from 2009 to 2018 were selected as well at the time interval of 6 h.

To compensate for the shortcoming of the uneven spatial distribution of the AWSs, this study also uses reanalysis data from the European Centre for Medium-Range Weather Forecasts (ECMWF) to compute the relation between the near land surface wind and the TBB. ERA5 is the fifth generation ECMWF atmospheric reanalysis of the global climate.

Reanalysis combines model data with observations from across the world into a globally complete and consistent dataset using physics laws [33]. In this study, the ERA5 hourly reanalysis data on the single level from June to September during the 2009–2018 period were used. The spatial resolution was 0.25° × 0.25°. The specific 551 hourly moments corresponding to the above TC periods were chosen out and the meteorological elements used are the meridional wind (10 m u-component of wind) and zonal wind (10 m v-component of wind) and wind gust (10 m wind gust since previous post-processing) at the 10 m level.

3. Methods

3.1. Sliding Window

The sliding window has an important application in data mining and extraction [34,35]. The goal of using sliding window segmentation is to find a set of cut points to partition the sequence of a variable into smaller subintervals. The sliding window size can be defined based on time or a selected number of samples. The variable values falling within the sliding window are scanned to determine the minimum or maximum applicable variable in subintervals [36]. In this study, we used sliding window technology to group the TBB sequence, and then determine the maximum wind speed and other percentile values within each TBB group, making the change of the maximum wind speed between successive groups smoother.

Given a series of T with length m, and a user-defined subsequence length of n, all possible subsequences can be extracted by sliding a window of size n across T [37]. The process of a sliding window is shown in Figure 3. For the series of (T_1, T_2, T_3, . . . , T_m), a sliding window of length n is set at the beginning of the series. The sliding window thus corresponds to (T_1, T_2, T_3, . . . , T_n). Then sliding window moves along the series by setting step-size s, corresponding to a sub-series of (T_{1+s}, T_{2+s}, T_{3+s}, . . . , T_{n+s}) [38]. Finally, we can get all subsequences and get the maximum value and some percentiles value for each subsequence.

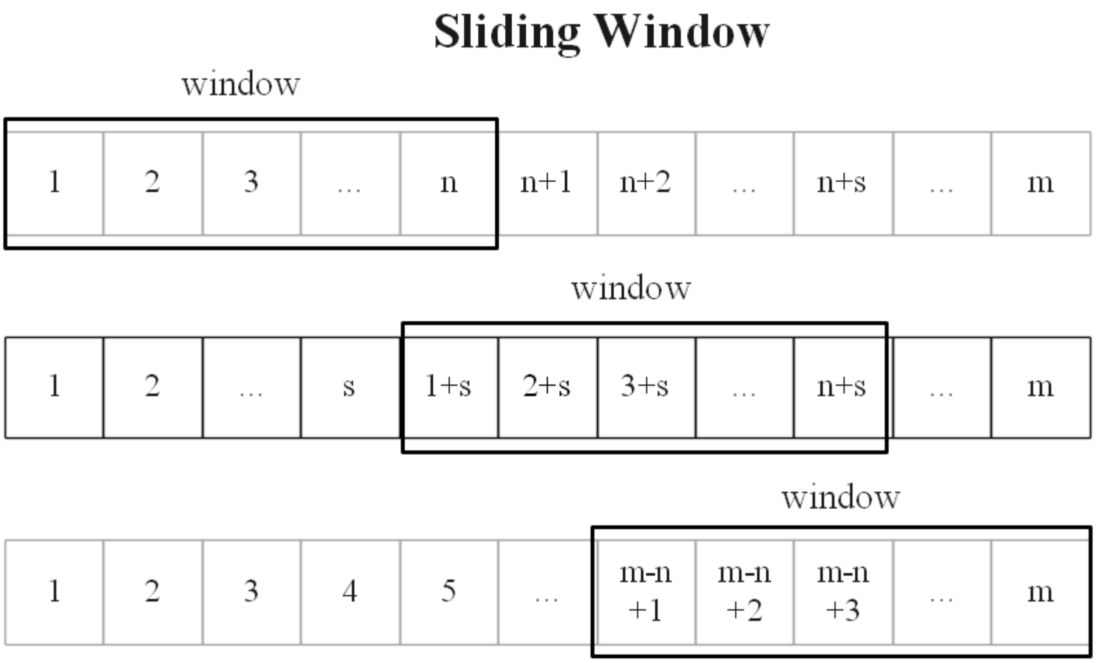

Figure 3. Scheme diagram for the process of a sliding window.

3.2. Correlation Analysis

The Pearson correlation coefficient was used to compute the correlation between the TBB and the wind speed at the AWS [39]:

$$r_{xy} = \frac{cov(X, Y)}{\sqrt{var(X)} \times \sqrt{var(Y)}} \tag{1}$$

where r_{xy} is the correlation coefficient between variables X and Y; $cov(X, Y)$ is the covariance of X, Y, and $var(X)$, $var(Y)$ are the variances of X and Y, respectively. The correlation significance between TBB and wind speed can be tested by the Student's T distribution. The critical correlation coefficient for identifying correlation significance can be obtained as follows [40]:

$$r_{crit} = \frac{t_{\alpha/2,n^*}}{\sqrt{t^2_{\alpha/2,n^*} + n^* - 2}} \tag{2}$$

here, the confidence level is chosen to be 95%, so $\alpha = 0.05$. $t_{\alpha/2,n^*}$ is the point in the Student's T distribution with n^* degrees of freedom that has a probability of exceedance of $\alpha/2$. When we had two autocorrelated variables, the effective degree of freedom n^* was computed as follows [41]:

$$n^* = \frac{n}{\sum_{\tau=-\infty}^{+\infty} [r_{xx}(\tau) r_{yy}(\tau) + r_{xy}(\tau) r_{yx}(\tau)]} \tag{3}$$

where n is the number of samples, τ is the lag time, and $r_{xx}(\tau)$, $r_{yy}(\tau)$ are the autocorrelation coefficients for TBBs and wind speeds, respectively. $r_{xy}(\tau)$ and $r_{yx}(\tau)$ refer to the cross correlations between TBBs and wind speeds. In reality, the computation of n^* requires a finite lag instead of infinite long (∞) [41]. The simplest case is the presence of lag 1 autocorrelation in short series, widely used in much of studies [42–45]. So, we used lag 1 to estimate the effective degree of freedom in this study. If $|r_{xy}| > r_{crit}$, we consider there's a significant correlation between X and Y.

3.3. Least Square Fitting

Least-squares regression is used to fit the line between the TBBs and the wind gusts or the average-wind speeds observed at the stations in Guangdong. The regression equation is shown below:

$$V = A \times (X - X0) + B \tag{4}$$

where V is the wind speed, X is the TBB (K) value, and $X0$ is a specified reference TBB. A and B are constants. R^2, the coefficient of determination, is used to check the goodness of fitting [46].

4. Results and Discussion

As mentioned in the data section, there were 23 TCs making their first landfall along the coast of Guangdong Province from 2009 to 2018. Among them, Vicente (2012), Hato (2017), and Mangkhut (2018) are three typhoons that attacked the Pearl River Delta, causing intense wind and severe damage along the coast [47]. When Vicente made landfall, the maximum 2-min average wind near the center was 40 m/s (grade 13) (based on the Beaufort scale, which is the same hereafter), and the minimum pressure in the center was 955 hPa. Under the influence of Vicente, strong wind gusts of grade 11–13 appeared on the coast and sea of Guangdong Province, among which the highest gust of 44.6 m/s (grade 14) was recorded in Shangchuan Island town [48]. Hato made landfall with a maximum 2-min average wind of 45 m/s (grade 14) near the TC center and a minimum pressure of 950 hPa. During the Hato landfall period, average wind speeds of grade 11–14 appeared in coastal areas of the Pearl River Delta, with gusts reaching grade 16–17 in Zhuhai, Macao, Hong Kong, and the Pearl River Estuary. The maximum recorded wind gust was in Guishan Island, Zhuhai with the value of 66.9 m/s (grade 17) [49]. When Mangkhut landed, the center had a maximum 2-min average wind speed of 45 m/s and a minimum pressure of

955 hPa [50]. The strong wind caused by Mangkhut had the characteristics of a wide range and long duration. Hong Kong, Macau, Shenzhen, and Zhuhai generally had the average wind speeds of grade 13–14 and gusts of grade 16–17. The duration of the wind gust above grade 12 in the Pearl River Delta coastal area lasted more than 16 h [51].

Figure 4 shows the satellite images of Vicente, Hato, and Mangkhut when making landfall in Guangdong. The red solid lines in the figure refer to the isolines with a TBB of 210 K, and the red points within the isolines represent the TCs centers. The whole range of the TC cloud system, the spiral TC cloud belt, the cloud wall around the eye, and the asymmetrical distribution of the vigorous convective cloud area around the TC eye can be seen from the figure. The TC cloud structure is tight and the TBB of the TC cloud is much lower than that of the surrounding cloud [52]. The stations' locations with the recorded wind gusts greater than grade 12 ($\geq$32.7 m/s) when the three TCs making landfall are marked with white points in Figure 4. We can see that all these white points are mostly located to the northeast of the TCs centers and are close to the TC centers. All the TBBs of the cloud area corresponding to the location of the white points are low. However, it is not certain that all locations at low TBB areas can be observed with strong wind gusts. We cannot directly inverse the near-surface wind speeds by the TBBs. The relationship between the TBBs from the satellite images and the near-surface wind speeds at stations is worthy of investigation.

As mentioned before, the hourly observations at the AWSs 12 h before and after TCs landfall are selected to explore the potential TC wind disaster. There are 551 hourly observation data available for the 23 TCs. Figure 5 shows the counts of the strong wind gusts at AWSs in Guangdong Province influenced by these 23 landfalling TCs. During the TCs landfalling period from 2009 to 2018, 279 stations had wind gusts greater than grade 12 ($\geq$32.7 m/s). As can be seen from the figure, the stations located in the Pearl River Delta area had more times with gusts greater than 32.7 m/s. Among those 279 stations, 24 stations had more than 11 ($\geq$11) times that wind gusts were greater than 32.7 m/s. Among the 24 stations, Yantian International Container Terminal (YICT) is a natural deep-water terminal and the leading gateway serving import and export container traffic [29]. As the largest and busiest container terminal in Southern China, YICT's daily operations rely heavily on weather conditions, especially wind conditions. So, it is crucial to provide accurate meteorological services for ports and harbors, especially the early warning and forecast services under the TCs' influence [53]. Bei Zai Jiao (BZJ) is an important nearby reference station for YICT. Besides the 24 stations with more than 11 times wind gusts greater than 32.7 m/s, BZJ, which has 8 times of wind gusts observation greater than grade 12, was also used to explore the potential wind disaster induced by TCs. The information of all these 25 stations is shown in Table 1.

YICT (G3567) was taken as a representative station to analyze the relationship between TBBs and the wind speeds at the station. Figure 6 shows the scatter plots of the observed gusts (a) and average-winds (b) with the corresponding TBBs at YICT from 2009 to 2018. Blue points refer to the wind observations during TC periods and yellow points refer to the observations at a 6-h interval from June to September during the study period when there is no TC. As shown in the figure, the scopes of average-winds and gusts are wide for a given TBB. For example, for the TBB of 200 K in Figure 6, the range of gust at YICT during TC periods was from 9 to 33 m/s, and the range of average-wind at YICT during TC periods was from 6 to 24 m/s. The TBBs cannot determine the speeds of the average wind and gust at a specific station. However, there is an upper limit of observed average-wind and gust for a given TBB.

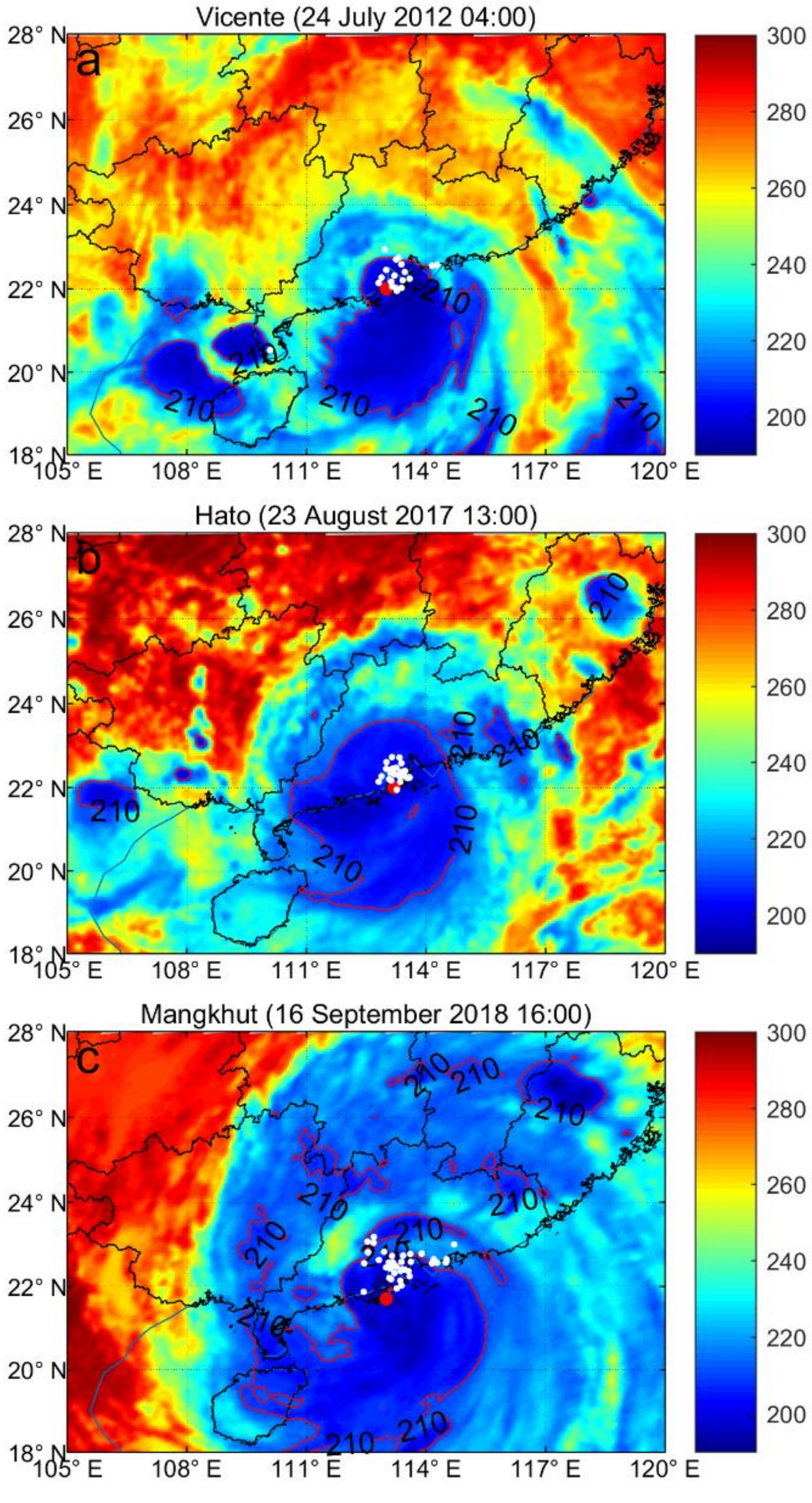

Figure 4. The satellite images when the Vicente (**a**), Hato (**b**), and Mangkhut (**c**) making landfall in Guangdong. The red solid lines refer to the isolines with a black body temperature (TBB) of 210 K, and the red points within the isolines represent the TCs centers. The white points refer to the stations' locations with the recorded wind gusts greater than grade 12 ($\geq$32.7 m/s).

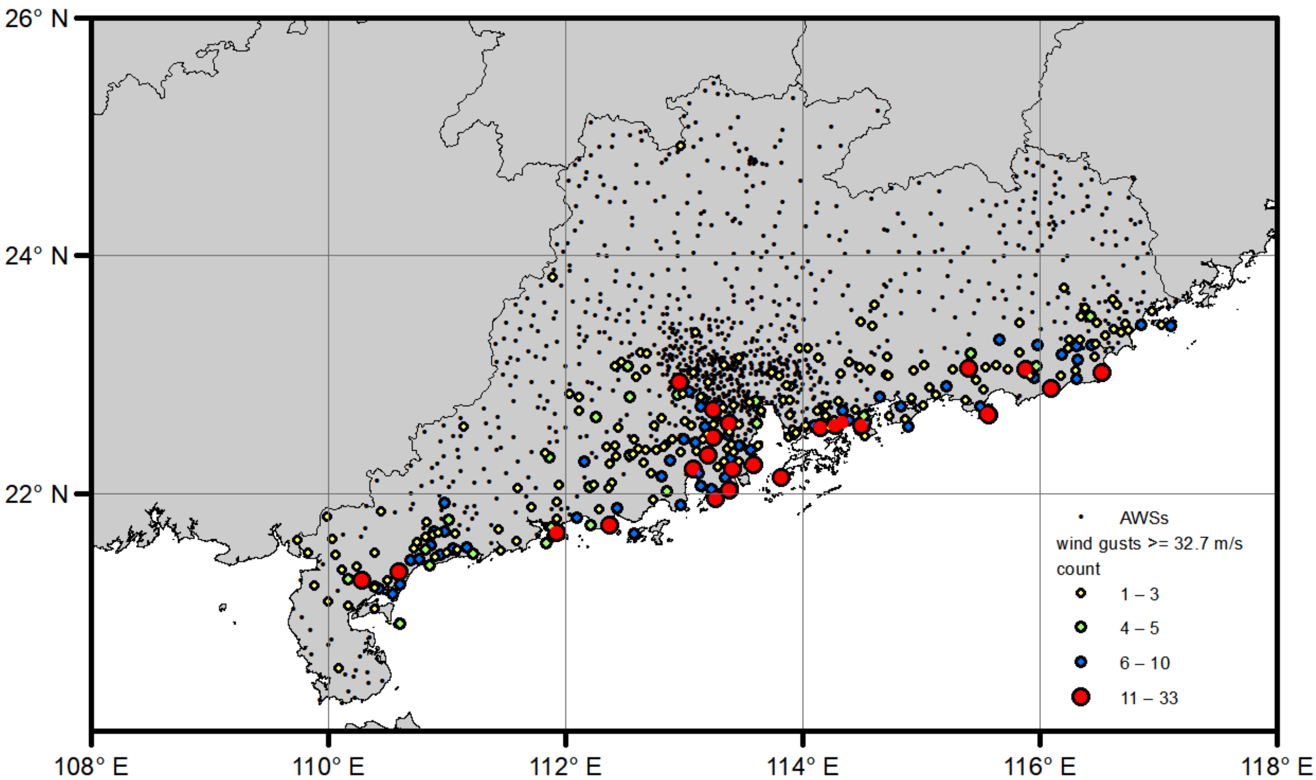

Figure 5. The counts of the strong wind gusts at AWSs in Guangdong Province influenced by the 23 landfalling TCs from 2009 to 2018. Different color refers to the different times that wind gusts at the AWS are greater than grade 12 (≥32.7 m/s) during the TCs landfalling period.

Table 1. The information of the 25 representative stations, arranged in the alphabetical order of the weather stations' name.

OBTID	Station Name	Abbreviation	Longitude	Latitude
G3536	Bei Zai Jiao	BZJ	114.3	22.6
G2185	Beidouzhen Naqinxu	NQX	112.4	21.7
G2425	Deyu Jidi	DYJD	110.3	21.3
G2012	Dongfengzhen	DFZ	113.3	22.7
59682	Gao Lan Dao	GLD	113.3	22.0
G1820	Gongping Shuiku	GPSK	115.4	23.1
G1201	Gui Shan Dao	GSD	113.8	22.1
G2310	Hailing Dadi	HLDD	111.9	21.7
G1251	Hengshan	HS	113.2	22.3
G1805	Honghaiwan	HHW	115.6	22.7
G2451	Huangpozhen Caizhengsuo	HPZCZS	110.6	21.3
G1833	Jiadongzhen	JDZ	116.1	22.9
G2950	Jinghaizhen	JHZ	116.5	23.0
G1209	Jiuzhougang	JZG	113.6	22.2
G3525	Longqi	LQ	114.5	22.6
G3524	Luohu Dangxiao	LHDX	114.2	22.6
G1206	Nanping Guangchang	NPGC	113.4	22.2
G1838	Piyangzhen	PYZ	115.9	23.0
G2046	Quanlucun	QLC	113.3	22.5
G2017	Shenwan Dapaicun	SW	113.4	22.6
G1811	Shunzhou Baoyuchang	SZBYC	115.6	22.7
G6868	Xiqiao Shanding	XQ	113.0	22.9
G2111	Ya Nan Shuilihui	YNSLH	113.1	22.2
G3567	Yantian International Container Terminal	YICT	114.3	22.6
G1205	Zhuhai Jichang	ZHJC	113.4	22.0

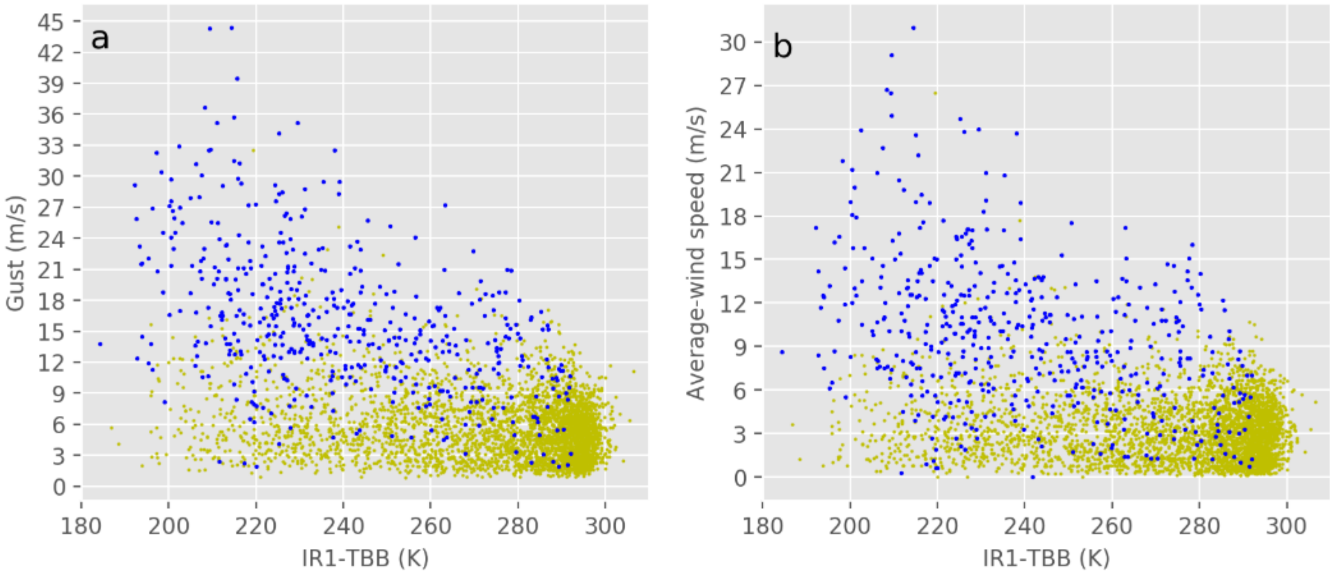

Figure 6. Scatter plots of the gusts (**a**) and average-winds (**b**) with the corresponding TBBs at the Yantian International Container Terminal (YICT) from 2009 to 2018. Blue points refer to the observations during TC periods, and yellow points refer to the observations at a 6-h interval from June to September during the study period when there is no TC.

The relationship between TBBs and the wind speeds was similar to the relationship between the sea surface temperature (SST) and TC intensity. Merrill [54] suggested that a wide range of intensities is observed over a given range of SSTs. The SSTs are more likely to be a capping function of the TC's intensity rather than a direct predictor of intensity. DeMaria and Kaplan [55] developed an empirical relationship between climatological SST and the maximum sustained winds of the Atlantic TCs from 1962 to 1992. Their studies indicated that an exponential function was fit to predict the MPI (maximum potential intensity) of a TC. Whitney and Hobgood [56] found the empirical maximum potential intensity relationship for TCs over the eastern North Pacific Ocean was a linear function compared with an empirical relationship over the Atlantic Ocean. Additionally, some other studies [57,58] had also explored the upper limit function between SST and MPI.

The relationship between TBBs and the gusts or the average-winds at the station was similar. We could find a capping function to predict the maximum potential gusts and maximum potential average-winds of TCs with the 10-year observations. To determine the capping function of the gusts and average-winds with a given range of the TBBs, we grouped the TBBs by the sliding window of size 10 and the sliding interval of 5. Taking YICT as an example again, the historical TBB observations from 195 to 310 K at the station were divided into 22 groups, as indicated in Table 2. Except for the group above 300 K, the difference between the average TBB and the TBB midpoint in each group was less than 1 K. For the sake of simplification, we used the midpoint value of TBB in each group to represent the group. Each sample was assigned to the nearest TBB group. Since only ten TBBs at YICT were less than 195 K, those observations were included in the 200 K group to prevent a possible analysis bias due to a few low TBBs [56].

Among the 23 TCs studied in this paper, Mangkhut (2018) is the most intense one. YICT had the maximum wind gust observation of 44.4 m/s during the Mangkhut landfalling period. Figure 7 shows the curves for the maximum, 99th, 95th, 90th, and 50th percentiles of the hourly wind gusts (a) and average-winds (b) for every TBB group at YICT. The top four curves, i.e., the maximum hourly observation, 99th, 95th, and 90th percentile hourly wind speeds, decreased sharply when TBBs were above 215 K, while the median (50th percentile) curve varied slowly as a function of TBB.

Table 2. Information of the TBB groups corresponding to the wind observations at YICT.

TBB Midpoint (K)	Number of Observations	Average TBB (K)	Maximum Gust (m/s)	Maximum Average-Wind Speed (m/s)
200	69	200.49	32.9	23.9
205	101	205.47	44.3	29.1
210	146	210.61	44.4	31.0
215	189	215.32	44.4	31.0
220	223	220.3	32.5	26.5
225	252	225.22	35.2	24.7
230	261	229.97	35.2	24.7
235	258	234.91	32.5	23.7
240	256	240.13	32.5	23.7
245	257	245.12	25.7	15.3
250	301	250.36	25.7	17.5
255	353	255.11	25.2	17.5
260	372	260.11	27.2	17.2
265	402	265.18	27.2	17.2
270	457	270.36	22.8	14.7
275	519	275.24	21.0	16.0
280	674	280.64	21.0	16.0
285	1038	285.74	18.0	14.0
290	1738	290.85	17.1	12.2
295	1711	294.09	13.7	10.7
300	656	296.95	11.8	7.4
305	49	301.31	11.7	6.6

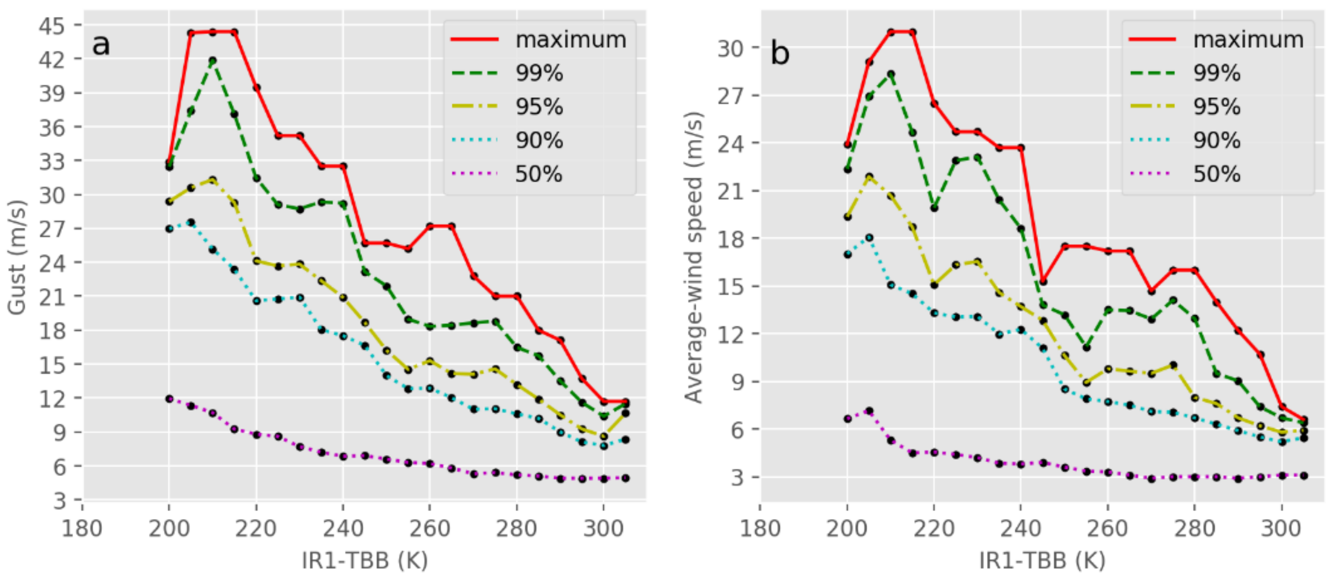

Figure 7. Curves of the maximum, 99th, 95th, 90th, and 50th percentiles of the hourly wind gusts (**a**) and average-winds (**b**) for each TBB group at YICT. The X coordinate refers to the midpoint value of TBB in each group, and the Y coordinate refers to the hourly wind gust and average-wind, respectively.

The Pearson correlation coefficient and Student's T distribution were applied to test the correlation between TBBs and the maximum wind speeds. We took YICT, for example, to explain the detailed process. The variable X refers to the TBB midpoint value for each TBB group as shown in Table 2. The variable Y refers to the maximum gust for each group in the table. The correlation coefficient r_{xy}, which can be calculated by Formula (1), is −0.95 at YICT. Additionally, $r_{xx}(\tau)$ and $r_{yy}(\tau)$ are the autocorrelation coefficients with the lag time τ for the TBBs and wind gusts, respectively. $r_{xy}(\tau)$ and $r_{yx}(\tau)$ are the cross correlations with the lag time τ between TBBs and wind gusts. They are used to calculate the effective degree of freedom n*, which is computed by Formula (3). n is the sample number, which is 22 for all stations, and the lag time is 1 in this study. The TBB midpoint values are the same for all stations and this variable series is linear, so $r_{xx}(1)$ is 1 for all stations. $r_{yy}(1)$ is computed to be 0.94, $r_{xy}(1)$ is computed to be -0.95, and $r_{yx}(1)$ is computed to be -0.94 for the wind gust at YICT. n* is computed to be 11.82 at YICT by Equation (3). In this paper, the confidence level was chosen to be 95%, so $\alpha = 0.05$. The $t_{\alpha/2,n^*}$ was 2.18 by looking up the Student's T distribution table with a 95% confidence level at YICT. Then the critical correlation coefficient r_{crit} was calculated by Formula (2), which was 0.57 for the wind gust at YICT. The absolute value of the correlation coefficient (-0.95) was more than the critical correlation coefficient (0.57) at YICT; therefore, there was a significant negative correlation between TBBs and the maximum gusts at YICT. All the computed results of the correlation coefficients, effective degrees of freedom, and critical correlation coefficients for the 25 representative stations are listed in Table 3. It can be found from the table that the absolute values of the correlation coefficients between TBBs and the maximum gusts or average-winds were greater than the corresponding critical correlation coefficients at all the 25 representative stations. Therefore, there were significant negative correlations between TBBs and the maximum gusts or the maximum average-winds at all the 25 stations.

Table 3. Correlations between TBBs and the maximum wind observations (including wind gusts and average-wind speeds) for the 25 representative stations.

	Gust (m/s)			**Average-Wind Speed (m/s)**		
Station	**r**	**n***	**r_{crit}**	**r**	**n***	**r_{crit}**
BZJ	−0.95	11.97	0.57	−0.97	11.58	0.58
NQX	−0.94	12.32	0.56	−0.85	13.40	0.54
DYJD	−0.90	12.44	0.56	−0.87	12.95	0.55
DFZ	−0.93	12.29	0.56	−0.89	13.63	0.53
GLD	−0.92	12.91	0.55	−0.89	13.51	0.54
GPSK	−0.93	12.76	0.55	−0.86	14.49	0.52
GSD	−0.95	11.72	0.57	−0.97	11.58	0.58
HLDD	−0.96	12.06	0.57	−0.94	12.12	0.57
HS	−0.94	12.26	0.56	−0.90	12.49	0.56
HHW	−0.94	12.80	0.55	−0.95	12.01	0.57
HPZCZS	−0.95	12.11	0.57	−0.93	12.60	0.55
JDZ	−0.93	12.21	0.56	−0.9	12.86	0.55
JHZ	−0.88	12.99	0.55	−0.88	13.01	0.55
JZG	−0.89	12.78	0.55	−0.95	12.09	0.57
LQ	−0.94	12.30	0.56	−0.96	11.82	0.57
LHDX	−0.95	12.09	0.57	−0.93	12.38	0.56
NPGC	−0.91	12.66	0.55	−0.81	14.99	0.51
PYZ	−0.94	12.84	0.55	−0.9	13.63	0.53
QLC	−0.93	12.19	0.56	−0.88	13.12	0.54
SW	−0.91	12.62	0.55	−0.9	12.94	0.55
SZBYC	−0.97	11.96	0.57	−0.95	12.52	0.56
XQ	−0.91	12.42	0.56	−0.79	14.63	0.52
YNSLH	−0.90	13.04	0.55	−0.86	13.65	0.53
YICT	−0.95	11.82	0.57	−0.94	12.07	0.57
ZHJC	−0.87	13.23	0.54	−0.89	14.19	0.52

Similar to the study of the relationship between the SST and the maximum intensities of TCs over the Eastern North Pacific Ocean [56], a least-squares regression was used to fit the line between the TBBs and the maximum wind gusts or the maximum average-wind speeds at those representative stations. Based on Equation (4), X0 was set to be 180 K, which is the minimum TBB. The constants in Equation (4) were computed by the least-squares regression. Figure 8 shows the fitting lines between the TBBs and the maximum wind gusts (a), and between the TBBs and the maximum average-wind speeds (b) at YICT. In the remaining of this paper, the wind gust calculated by Equation (4) is referred to as the maximum potential gust (MPG) and the average-wind calculated by Equation (4) is referred to as the maximum potential average-wind (MPAW). Similar to the study of Whitney and Hobgood [56], which excluded the maximum SST group in the best-fit computation, we also found the fitting lines of the maximum wind gusts and the maximum average-wind speeds that excluded the minimum TBB group of 200 K that were better than the lines with the 200 K group. As shown in Figure 8, the initial lines that include the 200 K category generally underestimated the maximum wind speeds when TBBs were less than 270 K, compared with the lines that did not include the data of the 200 K category. The constants A and B were −0.30 and 49.37, and R^2 was 0.90 for the fitting line with the 200 K group of the wind gusts at YICT. Additionally, the constants A and B were −0.33 and 52.12, and R^2 was 0.96 for the fitting line without the 200 K group of the wind gusts at YICT. The constants A and B were −0.21 and 34.09, and R^2 was 0.88 for the fitting line with the 200 K group of the average-wind speeds at YICT. Additionally, the constants A and B were −0.22 and 35.68, and R^2 was 0.92 for the fitting line without the 200 K group of the average-wind speeds at YICT. The R^2 of the fitting lines without the 200 K group for both wind gusts and average-wind speeds at YICT was larger than that of the fitting lines with the wind data of the 200 K group. Therefore, the fitting lines without the 200 K were used to represent the fitting results of the MPG and MPAW.

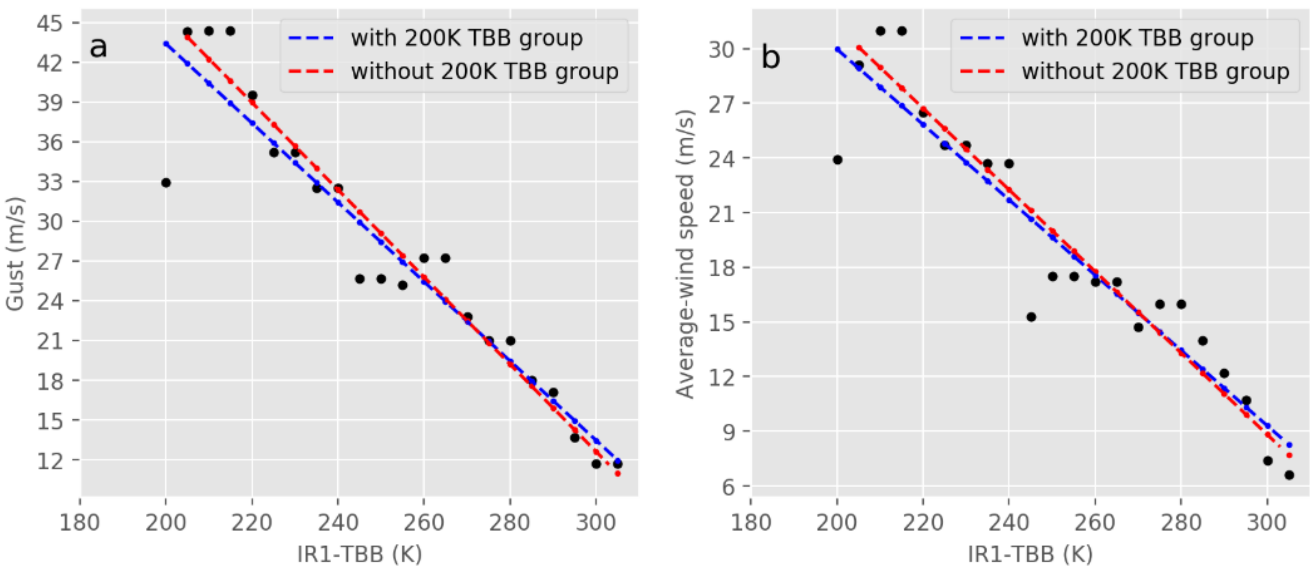

Figure 8. Comparison of best-fit lines with and without the 200 K TBB group for the maximum gusts (**a**) and for the maximum average-wind speeds (**b**) at YICT.

Figure 9 shows the fitting lines without the 200 K group computed by formula (4) and all the observations used in the analyses at YICT. As shown in the figure, the MPG and MPAW can provide reasonable estimates for the maximum observed gusts and average-wind speeds at YICT induced by landfalling TCs.

Similar to the YICT station, the MPG and MPAW at the other 24 representative stations were computed according to Equation (4). Table 4 shows the fitting parameters of all representative stations. It can be seen from the parameters that the MPG and MPAW of different stations were different, even though the stations were close to each other. For example, BZJ (G3536) and YICT (G3567) were all located in Yantian District, Shenzhen. The distance between them was 7.08 km. However, due to the influence of the topography and surrounding environment, the wind induced by TCs was generally greater at YICT than that at BZJ, though they might have a similar TBB at the same time. Figure 10 shows the comparison of the MPG and MPAW between the two stations. As shown in the figure, the computed MPG and the MPAW are generally greater at YICT than those at BZJ.

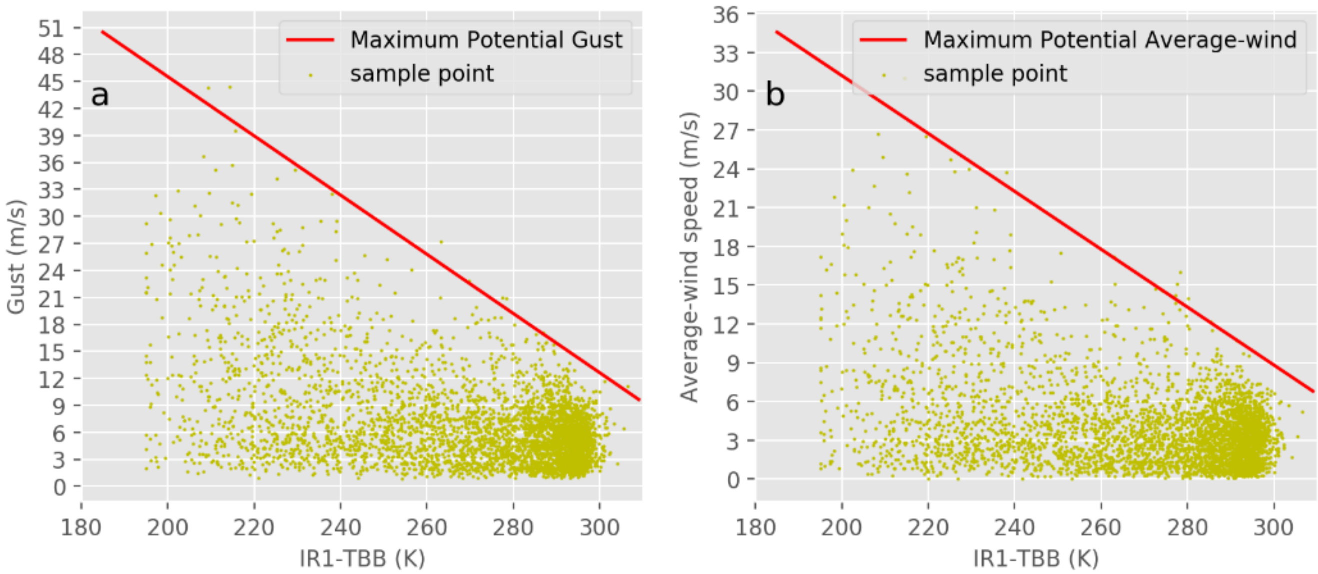

Figure 9. The scatter plot of the TBBs and the wind gusts from 2009 to 2018 at YICT and the fitted line for the maximum potential gust for the station (**a**); same as Figure 9a, but for the average-winds at YICT (**b**).

Table 4. The parameters of the fitting lines for the maximum potential gust (MPG) and maximum potential average-wind (MPAW) at the 25 stations.

	Gust (m/s)			Average-Wind Speed (m/s)		
Station	**A**	**B**	**R^2**	**A**	**B**	**R^2**
BZJ	−0.23	40.37	0.90	−0.16	25.26	0.93
NQX	−0.31	48.97	0.89	−0.20	30.63	0.72
DYJD	−0.32	47.67	0.82	−0.20	28.84	0.76
DFZ	−0.29	56.93	0.87	−0.17	30.43	0.79
GLD	−0.36	59.17	0.84	−0.22	38.01	0.78
GPSK	−0.35	53.09	0.86	−0.22	33.20	0.74
GSD	−0.28	46.65	0.78	−0.18	29.04	0.82
HLDD	−0.25	44.66	0.91	−0.17	32.03	0.89
HS	−0.30	47.81	0.88	−0.18	28.45	0.82
HHW	−0.42	64.13	0.88	−0.24	37.63	0.91
HPZCZS	−0.24	43.67	0.90	−0.16	26.31	0.86
JDZ	−0.26	46.85	0.86	−0.18	31.33	0.81
JHZ	−0.33	52.50	0.78	−0.22	33.75	0.77
JZG	−0.32	50.21	0.79	−0.19	32.87	0.90
LQ	−0.28	49.44	0.88	−0.16	26.38	0.92
LHDX	−0.27	47.15	0.91	−0.13	24.26	0.86
NPGC	−0.23	44.43	0.84	−0.16	29.23	0.66
PYZ	−0.34	54.72	0.88	−0.21	33.17	0.81
QLC	−0.34	47.18	0.86	−0.21	28.64	0.78
SW	−0.28	46.87	0.84	−0.15	25.45	0.81
SZBYC	−0.36	56.19	0.93	−0.24	37.57	0.90
XQ	−0.27	47.86	0.83	−0.11	19.43	0.63
YNSLH	−0.35	48.94	0.81	−0.25	33.53	0.75
YICT	−0.33	52.12	0.96	−0.22	35.68	0.92
ZHJC	−0.29	47.13	0.76	−0.14	25.98	0.79

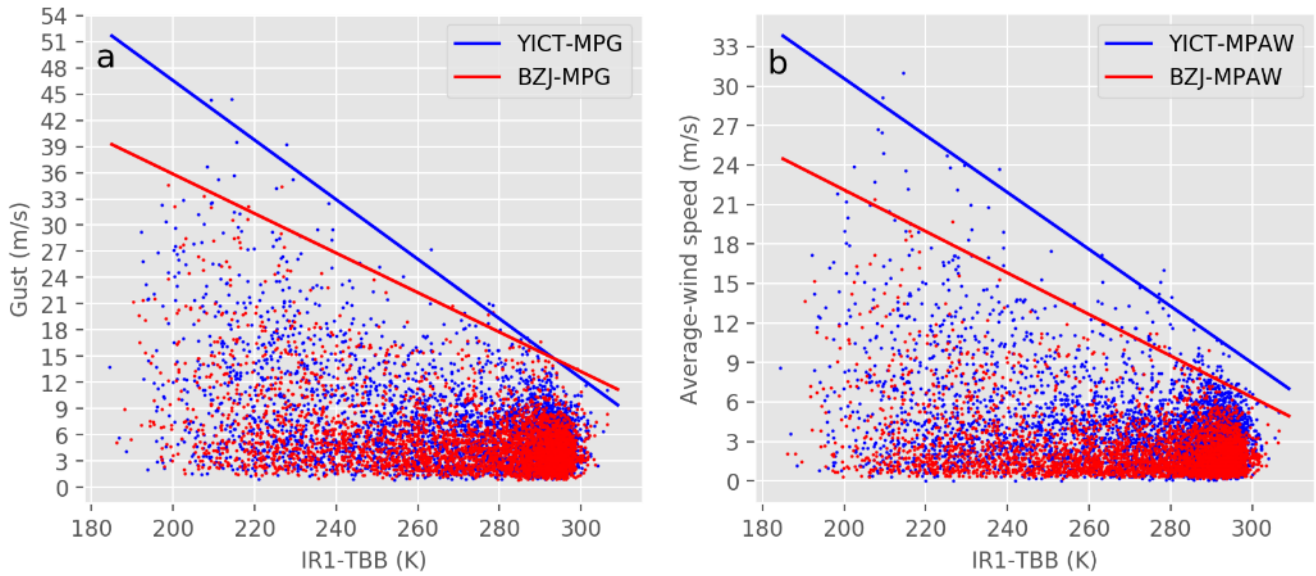

Figure 10. Comparison of the MPG (**a**) and MPAW (**b**) between YICT (G3567) and Bei Zai Jiao (BZJ, G3536).

Considering the unevenly spatial distribution of the weather stations, we used ERA5 reanalysis data for further study. The reanalysis data can make up for the shortage of observation in the remote area. The specific elements used were the hourly maximum 10 m wind gust and 10 m average-wind. To investigate similarities and discrepancies between the wind observations and the corresponding reanalysis data, the observed wind speeds at a representative station were compared with the wind speeds from the closest reanalysis grid. We assumed that this closest series matches the observed data better than any other series from more distant grid points [59]. From the longitude and latitude of the station, YICT and BZJ match the same grid. The comparisons between the measured wind speeds at the two stations and reanalysis data of the corresponding grid are shown in Figure 11.

As shown in Figure 11a, the scatter points of wind gusts at YICT were distributed almost uniformly on both sides of the line y = x. More scatter points of the wind gusts at BZJ were below the line of y = x. For the average-wind (Figure 11b), more scatter points for YICT were above the line of y = x; while more scatter points for BZJ were below the line of y = x. However, the scatter plots of the points for YICT and BZJ were uniformly distributed along the line of y = x. Thus, the wind speeds of the nearest grids from the reanalysis data can generally represent the average wind conditions of the two weather stations. Then we further explored the relationship between TBBs and the 10 m wind gusts or the 10 m average-winds of reanalysis data from 2009 to 2018.

Figure 12 shows the scatter plot of TBBs and the wind gusts (Figure 12a) or average-wind speeds (Figure 12b) from the reanalysis data for the nearest grid of YICT (and BZJ). As can be seen in Figure 12, the relationship between the TBBs and the wind gusts or average-wind speeds of the reanalysis data resembles the relationship between the TBBs and the observed wind speeds at stations. Similarly, we fitted the maximum potential wind gusts and the maximum potential average-wind speeds of the reanalysis data using Equation (4). The fitting lines are also shown in Figure 12. The result suggests that the historical TBBs of a certain grid point can determine the upper limits of the 10 m wind gusts or the 10 m average-wind speeds over the grid area.

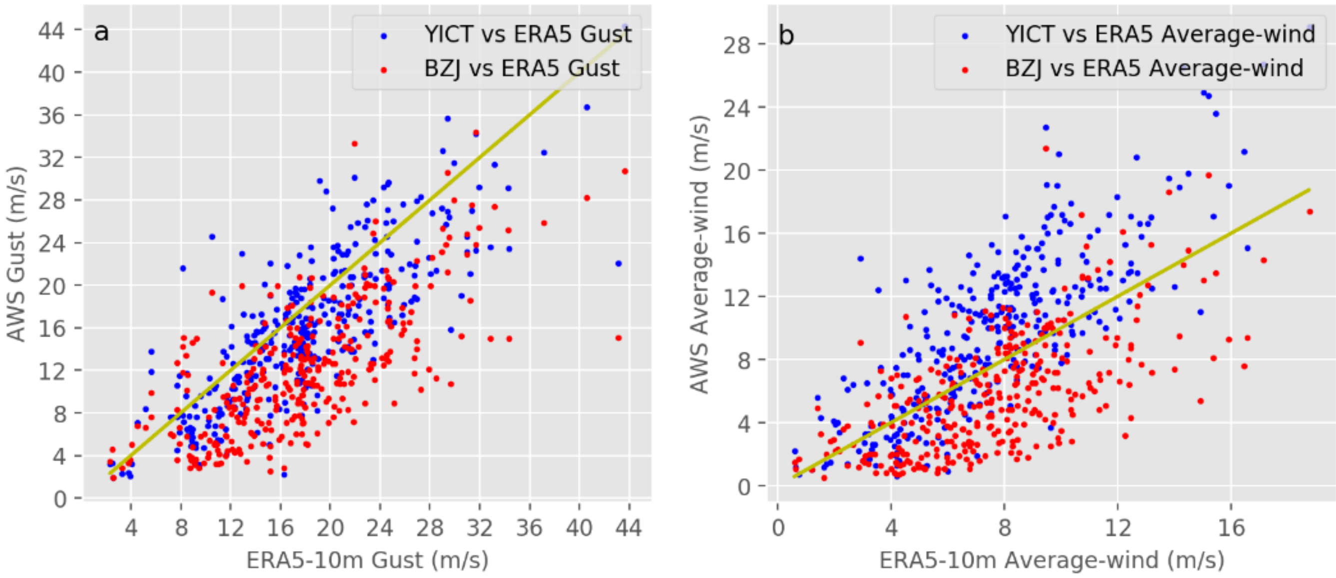

Figure 11. Comparisons of the wind gusts (**a**) and average-winds (**b**) between the observations at the stations and the reanalysis data of the closest grid. The X coordinate refers to the reanalysis data, and the Y coordinate refers to the observations. Red points are for BZJ, and blue points are for YICT. The brown line is for y = x.

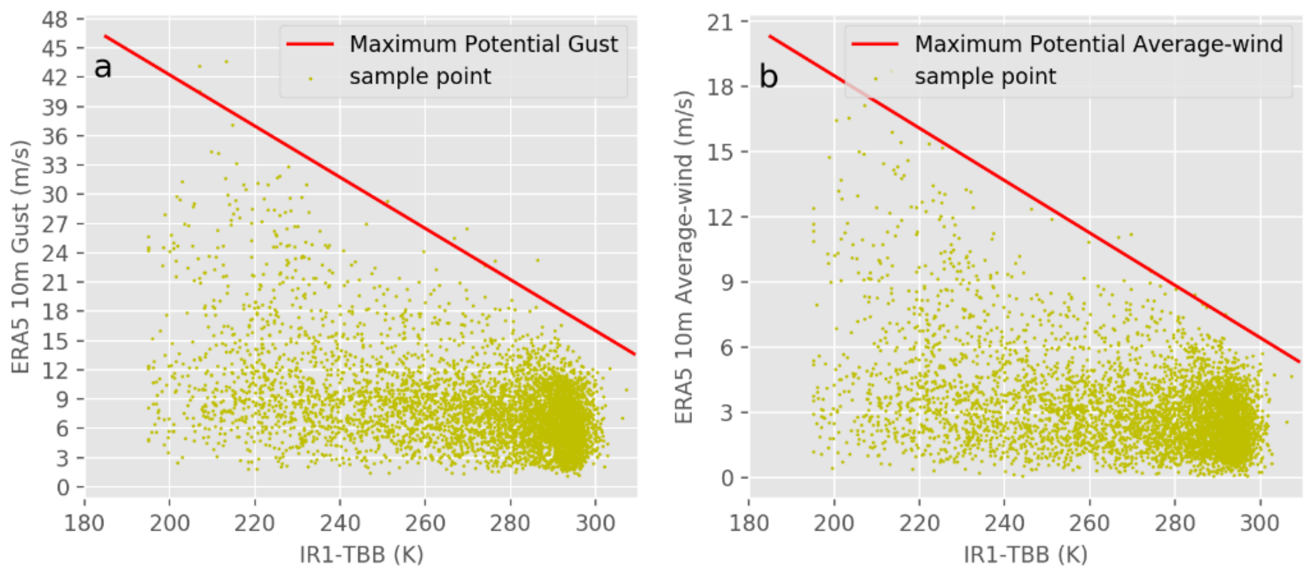

Figure 12. Scatter plot of TBBs and the wind gusts (**a**) and average-wind speeds (**b**) from the reanalysis data for the nearest grid of YICT (and BZJ) from 2009 to 2018. The fitted lines of the MPG (**a**) and MPAW (**b**) are also shown in the figure.

We also computed the MPGs and MPAWs for other grids that are close to the representative stations using Equation (4). Table 5 shows the calculated parameters of all grids. It can be seen that the differences in the parameters of MPG and MPAW between different grids were less than the differences between different stations. For example, the slope of the fitting line was −0.33 for the wind gusts at YICT, and the slope of the fitting line was −0.42 for the wind gusts at HHW; the slope of the fitting line was −0.26 for the wind gusts at the nearest reanalysis grid of YICT, and the slope of the fitting line was −0.28 for the wind gusts at the nearest reanalysis grid of HHW. The difference of slopes between the two reanalysis grids was less than the difference between the two stations. Therefore, the reanalysis data can represent an average condition over a region and can provide a general supplement for the area, which lacks weather stations; however, it cannot reflect the extreme condition in a region.

Table 5. The parameters of the fitting lines for the MPGs and MPAWs at the nearest grids of the 25 stations based on the ERA5 reanalysis data.

Station	Longitude	Latitude	Gust (m/s)			Average-Wind (m/s)		
			A	B	R^2	A	B	R^2
BZJ (YICT, LHDX)	114.25	22.5	−0.26	47.5	0.88	−0.12	20.92	0.94
NQX	112.5	21.75	−0.22	41.51	0.9	−0.12	24.09	0.83
DYJD	110.25	21.25	−0.2	38.73	0.84	−0.09	18.51	0.85
DFZ	113.25	22.75	−0.27	43.63	0.9	−0.12	20.23	0.91
GLD	113.25	22	−0.22	41.57	0.92	−0.14	26.28	0.89
GPSK	115.5	23	−0.23	43.19	0.78	−0.1	18.52	0.87
GSD	113.75	22.25	−0.27	46.34	0.78	−0.16	27.51	0.82
HLDD	112	21.75	−0.2	37.88	0.89	−0.12	21.55	0.9
HS	113.25	22.25	−0.26	43.3	0.95	−0.13	22.32	0.97
HHW (SZBYC)	115.5	22.75	−0.28	46.78	0.95	−0.17	27.66	0.97
HPZCZS	110.5	21.25	−0.22	42.38	0.85	−0.11	21.16	0.86
JDZ (PYZ)	116	23	−0.29	49.68	0.86	−0.14	23.8	0.91
JHZ	116.5	23	−0.27	47.78	0.89	−0.18	29.37	0.9
JZG (NPGC)	113.5	22.25	−0.27	45.35	0.95	−0.13	22.89	0.94
LQ	114.5	22.5	−0.31	52.57	0.86	−0.17	28.58	0.87
QLC	113.25	22.5	−0.26	43.48	0.91	−0.11	18.81	0.87
SW	113.5	22.5	−0.31	48.66	0.89	−0.14	22.48	0.92
XQ	113	23	−0.27	45.06	0.89	−0.14	22.95	0.85
YNSLH	113	22.25	−0.21	39.04	0.84	−0.09	18.32	0.82
ZHJC	113.5	22	−0.24	46.39	0.67	−0.13	28.17	0.73

5. Conclusions

Based on the historical TCs, which made their first landfall in Guangdong Province from 2009 to 2018, the hourly wind observations of AWSs in the province, and the TBBs data obtained from the infrared channel 1 (with the wavelength of 10.30–11.30 μm) of FY-2 satellite images, this study tried to explore the relationship between the near-surface wind speeds at the stations in Guangdong Province induced by landfalling TCs and the corresponding TBBs data. Twenty-five stations that generally suffer significantly during TCs' landfalling periods are applied as the representatives to explore the relationship.

The result shows that there is not a direct relationship between TBB and the wind observation at the AWSs. However, TBBs have significant negative linear relationships with the maximum wind gusts and the maximum average-wind speeds at the stations. TBBs can provide a capping function for the wind gusts and average-winds at the AWSs induced by TCs. The MPG and MPAW can provide reasonable estimates for the maximum observed gusts and average-wind speeds at the AWSs induced by TCs. Additionally, it was found that the parameters of MPG and MPAW were different at different stations due to the diverse terrain and surrounding environment of the AWS, even though the distance between the AWSs may be very close.

Furthermore, the relationship between the wind speeds of ERA5 reanalysis data during the ten years and the corresponding TBBs data is explored. Similarly, there is a negative linear relationship between the TBBs and the 10 m maximum wind gusts (or the maximum average-wind speeds) at the grids close to the representative stations. The differences in the parameters of the MPG and MPAW between different grids were generally less than the differences between the corresponding stations with strong wind observations. The reanalysis data can provide a good supplement for the area, which lacks weather stations; however, it cannot reflect the extreme condition in a region.

Author Contributions: Conceptualization, J.Z., Q.L., W.Z. and J.H.W.L.; Data curation, J.Z.; Formal analysis, J.Z., Q.L. and W.Z.; Funding acquisition, Q.L.; Investigation, J.Z. and Q.L.; Methodology, J.Z., Q.L. and W.Z.; Project administration, Q.L.; Resources, Q.L., J.L. and S.W.; Software, J.Z. and Q.L.; Supervision, Q.L.; Validation, J.Z., Q.L. and W.Z.; Visualization, J.Z.; Writing—original draft, J.Z. and Q.L.; Writing—review and editing, Q.L. and J.H.W.L. All authors have read and agreed to the published version of the manuscript.

Funding: This research was funded by the Science and Technology Department of Guangdong Province (grant 2019B111101002).

Institutional Review Board Statement: Not applicable.

Informed Consent Statement: Not applicable.

Data Availability Statement: The data presented in this study are available from China Meteorological Data Service Centre at the website of http://data.cma.cn (accessed on 10 April 2021) and from the European Centre for Medium-Range Weather Forecasts at the website of http://cds.climate.copernicus.eu (accessed on 10 April 2021).

Conflicts of Interest: The authors declare no conflict of interest.

References

1. Lei, X. Overview of the development history of China's typhoon research and operational work in the past century. *Sci. China Earth Sci.* **2020**, *63*, 362–383. [CrossRef]
2. Li, H.; Li, Q.; Huang, D.; Zhang, L.; Li, G.; Zhang, L.; Zhang, L.; Yang, Y. Wind Gust Forecast and Evaluation for Specific Locations Based on Historical Tropical Cyclone Data. *J. Trop. Meteorol.* **2019**, *35*, 652–663. (In Chinese)
3. Tan, C.; Fang, W. Mapping the wind hazard of global tropical cyclones with parametric wind field models by considering the effects of local factors. *Int. J. Disaster Risk Sci.* **2018**, *9*, 86–99. [CrossRef]
4. Yang, Y.; Lei, X. Statistics of strong wind distribution caused by landfall typhoon in China. *J. Trop. Meteorol.* **2004**, *6*, 633–642. (In Chinese)
5. Kaplan, J.; DeMaria, M. A simple empirical model for predicting the decay of tropical cyclone winds after landfall. *J. Appl. Meteorol.* **1995**, *34*, 2499–2512. [CrossRef]
6. Yan, D. *Research on Distribution Characteristics and Forecast for Tropical Cyclone Gale in Guangxi*; Nanning Normal University: Nanning, China, 2014. (In Chinese)
7. Zhang, Q.; Wu, L.; Liu, Q. Tropical cyclone damages in China 1983–2006. *Bull. Am. Meteorol. Soc.* **2009**, *90*, 489–496. [CrossRef]
8. Chou, J.; Dong, W.; Tu, G.; Xu, Y. Spatiotemporal distribution of landing tropical cyclones and disaster impact analysis in coastal China during 1990–2016. *Phys. Chem. EarthParts A/B/C* **2020**, *115*, 102830. [CrossRef]
9. Wang, H.; Xu, M.; Onyejuruwa, A.; Wang, Y.; Wen, S.; Gao, A.E.; Li, Y. Tropical cyclone damages in Mainland China over 2005–2016: Losses analysis and implications. *Environ. Dev. Sustain.* **2019**, *21*, 3077–3092. [CrossRef]
10. Jiang, Y.; Luo, Y.; Zhao, Z.; Tao, S. Changes in wind speed over China during 1956–2004. *Theor. Appl. Climatol.* **2014**, *99*, 421–430. [CrossRef]
11. Powell, M.D.; Uhlhorn, E.W.; Kepert, J.D. Estimating maximum surface winds from hurricane reconnaissance measurements. *Weather Forecast.* **2009**, *24*, 868–883. [CrossRef]
12. Piñeros, M.F.; Ritchie, E.A.; Tyo, J.S. Objective measures of tropical cyclone structure and intensity change from remotely sensed infrared image data. *IEEE Trans. Geosci. Remote Sens.* **2008**, *46*, 3574–3580. [CrossRef]
13. Wang, G.; Wang, K.; Han, W.; Wang, D.; Qiu, X. Typhoon Maria Precipitation Retrieval and Evolution Based on the Infrared Brightness Temperature of the Feng-Yun 4A/Advanced Geosynchronous Radiation Imager. *Adv. Meteorol.* **2020**, *2020*, 1–12. [CrossRef]
14. Lan, H.; Zhang, R.; Jiang, Y. Infrared rainfall estimation technique for small area and its use in very short-term weather forecasting. *J. Trop. Meteorol.* **2000**, *16*, 366–373.
15. Yu, H.; Zhang, X. Application of bright temperature (TBB) in tropical cyclone research. *China Sci. Technol. Inf.* **2009**, *23*, 26–27. (In Chinese)
16. Dvorak, V.F. Tropical cyclone intensity analysis and forecasting from satellite imagery. *Mon. Weather Rev.* **1975**, *103*, 420–430. [CrossRef]
17. Dvorak, V.F. *Tropical Cyclone Intensity Analysis Using Satellite Data*; US Department of Commerce, National Oceanic and Atmospheric Administration, National Environmental Satellite, Data, and Information Service: Silver Spring, MD, USA, 1984.
18. Velden, C.; Harper, B.; Wells, F.; Beven, J.L., II; Zehr, R.; Olander, T.; Mayfield, M.; Guard, C.; Lander, M.; Edson, R.; et al. The Dvorak tropical cyclone intensity estimation technique: A satellite-based method that has endured for over 30 years. *Bull. Am. Meteorol. Soc.* **2006**, *87*, 1195–1210. [CrossRef]
19. DeMaria, M.; Kaplan, J. A statistical hurricane intensity prediction scheme (SHIPS) for the Atlantic basin. *Weather Forecast.* **1994**, *9*, 209–220. [CrossRef]

20. DeMaria, M.; Zehr, R.M.; Kossin, J.P.; Knaff, J.A. The use of GOES imagery in statistical hurricane intensity prediction. In Proceedings of the 25th Conference on Hurricanes and Tropical Meteorology, San Diego, CA, USA, 28 April 2002; pp. 120–121.
21. Mueller, K.J.; DeMaria, M.; Knaff, J.; Kossin, J.P.; Vonder Haar, T.H. Objective Estimation of Tropical Cyclone Wind Structure from Infrared Satellite Data. *Weather Forecast.* **2006**, *21*, 990–1005. [CrossRef]
22. Knaff, J.A.; Slocum, C.J.; Musgrave, K.D.; Sampson, C.R.; Strahl, B.R. Using routinely available information to estimate tropical cyclone wind structure. *Mon. Weather Rev.* **2016**, *144*, 1233–1247. [CrossRef]
23. Kossin, J.P.; Knaff, J.A.; Berger, H.I.; Herndon, D.C.; Cram, T.A.; Velden, C.S.; Murnane, R.J.; Hawkins, J.D. Estimating hurricane wind structure in the absence of aircraft reconnaissance. *Weather Forecast.* **2007**, *22*, 89–101. [CrossRef]
24. Long, Z.; Yi, X. Study on inversing cloud motion wind from visible and infrared satellite image. In Proceedings of the 2010 Second IITA International Conference on Geoscience and Remote Sensing, Qingdao, China, 28–31 August 2010; Volume 1, pp. 506–509.
25. Le Marshall, J.F.; Leslie, L.M.; Spinoso, C. The Generation and Assimilation of Cloud-Drift Winds in Numerical Weather Prediction (gtSpecial IssueltData Assimilation in Meteology and Oceanography: Theory and Practice). *J. Meteorol. Soc. Jpn. Ser. II* **1997**, *75*, 383–393. [CrossRef]
26. Leese, J.A.; Novak, C.S.; Clark, B.B. An automated technique for obtaining cloud motion from geosynchronous satellite data using cross correlation. *J. Appl. Meteorol.* **1971**, *10*, 118–132. [CrossRef]
27. Xu, J.; Zhang, Q. Status review on atmospheric motion vectors-derivation and application. *J. Appl. Meteorol. Sci.* **2006**, *17*, 574–582. (In Chinese)
28. Liu, C.; Li, Q.; Zhao, W.; Wang, Y.; Ali, R.; Huang, D.; Lu, X.; Zheng, H.; Wei, X. Spatiotemporal Characteristics of Near-Surface Wind in Shenzhen. *Sustainability.* **2020**, *12*, 739. [CrossRef]
29. Li, Q.; Xu, P.; Wang, X.; Lan, H.; Cao, C.; Li, G.; Zhang, L.; Sun, L. An operational statistical scheme for tropical cyclone induced wind gust forecasts. *Weather Forecast.* **2016**, *31*, 1817–1832. [CrossRef]
30. Chen, L.; Luo, H.; Duan, Y.; Yu, H. An Overview of Tropical Cyclone and Tropical Meteorology Research Progress. *Adv. Atmos. Sci.* **2004**, *21*, 505–514. [CrossRef]
31. Duan, Y.; Chen, L.; Liang, J.; Wang, Y.; Wu, L.; Cui, X.; Ma, L.; Li, Q. Research progress in the unusual variations of typhoons before and after landfalling. *Acta Meteorol. Sin.* **2014**, *72*, 969–986.
32. Hu, T.; Wang, X.; Zhang, D.; Zheng, G.; Zhang, Y.; Wu, Y.; Xie, B. Study on typhoon center monitoring based on HY-2 and FY-2 data. *IEEE Geosci. Remote Sens. Lett.* **2017**, *14*, 2350–2354. [CrossRef]
33. Hersbach, H.; Bell, B.; Berrisford, P.; Hirahara, S.; Horányi, A.; Muñoz-Sabater, J.; Nicolas, J.; Peubey, C.; Radu, R.; Schepers, D.; et al. The ERA5 global reanalysis. *Q. J. R. Meteorol. Soc.* **2020**, *146*, 1999–2049. [CrossRef]
34. Ishak, W.H.W.; Ku-Mahamud, K.R.; Norwawi, N.M. Mining temporal reservoir data using sliding window technique. *Ciit Int. J. Data Min. Knowl. Eng.* **2011**, *3*, 473–478.
35. Yahmed, Y.B.; Bakar, A.A.; Hamdan, A.R.; Ahmed, A.; Abdullah, S.M.S. Adaptive sliding window algorithm for weather data segmentation. *J. Theor. Appl. Inf. Technol.* **2015**, *80*, 322.
36. Ruutu, J.P.O.; Kilkki, M.K. System and Method Employing Last Occurrence and Sliding Window Technique for Determining Minimum and Maximum Values. U.S. Patent 6,023,453, 8 February 2000.
37. Keogh, E.; Lin, J.; Lee, S.-H.; Van Herle, H. Finding the most unusual time series subsequence: Algorithms and applications. *Knowl. Inf. Syst.* **2007**, *11*, 1–27. [CrossRef]
38. Shi, Y.; Zhai, P.; Jiang, Z. Multi-sliding time windows based changing trend of mean temperature and its association with the global-warming hiatus. *J. Meteorol. Res.* **2016**, *30*, 232–241. [CrossRef]
39. Benesty, J.; Chen, J.; Huang, Y.; Cohen, I. *Pearson Correlation Coefficient [M]//Noise Reduction in Speech Processing*; Springer: Berlin/Heidelberg, Germany, 2009; pp. 1–4.
40. Li, Q.; Chen, J. Teleconnection between ENSO and climate in South China. *Stoch. Environ. Res. Risk Assess.* **2014**, *28*, 927–941. [CrossRef]
41. Chen, J.; Kumar, P. Role of terrestrial hydrologic memory in modulating ENSO impacts in North America. *J. Clim.* **2002**, *15*, 3569–3585. [CrossRef]
42. Arnau, J.; Bono, R. Autocorrelation and bias in short time series: An alternative estimator. *Qual. Quant.* **2001**, *35*, 365–387. [CrossRef]
43. Solanas, A.; Manolov, R.; Sierra, V. Lag-one autocorrelation in short series: Estimation and hypotheses testing. *Psicológica* **2010**, *31*, 357–381.
44. McCarthy, G.D.; Haigh, I.D.; Hirschi, J.J.M.; Grist, J.P.; Smeed, D.A. Ocean impact on decadal Atlantic climate variability revealed by sea-level observations. *Nature* **2015**, *521*, 508–510. [CrossRef]
45. Bretherton, C.S.; Widmann, M.; Dymnikov, V.P.; Wallace, J.M.; Bladé, I. The effective number of spatial degrees of freedom of a time-varying field. *J. Clim.* **1999**, *12*, 1990–2009. [CrossRef]
46. Liangbo, C.; Yaqing, Z. Study on curve fitting based on least square method. *J. Wuxi Inst. Technol.* **2012**, *11*, 52–55.
47. Yang, J.; Li, L.; Zhao, K.; Wang, P.; Wang, D.; Sou, I.M.; Yang, Z.; Hu, J.; Tang, X.; Mok, K.M.; et al. A Comparative Study of Typhoon Hato (2017) and Typhoon Mangkhut (2018)—Their Impacts on Coastal Inundation in Macau. *J. Geophys. Res. Ocean.* **2019**, *124*, 9590–9619. [CrossRef]
48. Fang, L.; Xia, G.; Lin, Z.; Mai, J. Cause Analysis of Territorial Rain Affection in South. *J. Meteorol. Res. Appl.* **2013**, *34*, 1–8+109. (In Chinese)

49. Liu, Q.; Fu, C.; Li, M.; Li, T. Storm surge forecast and numerical study of "Hato" Typhoon. *Mar. Forecast.* **2018**, *35*, 29–36. (In Chinese)
50. Song, X.; Zhang, W.; Zhou, J.; Li, Y. A Comparative Analysis of the Effect of Typhoons Hato and Mangkhut on the Wind and Rain in Zhaoqing. *Guangdong Meteorol.* **2020**, *42*, 23–26, 31. (In Chinese)
51. Zou, W.; Liu, F.; Guo, Z.; Pan, X. Analysis of Extreme Winds Caused by Mangkhut Diagnostic in Baiyun Airport. *Air. Traffic. Manag.* **2019**, *8*, 68–71. (In Chinese)
52. Li, S.; Lai, S.; Xiong, Z.; Wang, T. Structural Changes and Precipitation Cloud Characteristics of Typhoon No.1822 Based on Satellite Cloud Images. *J. Shaoguan Univ. Nat. Sci.* **2019**, *40*, 49–53. (In Chinese)
53. Wang, Y.; Li, Q.; Lan, H.; Sun, L.; Cao, Y.; Li, G. Forecast of Maximum Wind Gust in Tropical Cyclones for Port Terminals in Shenzhen. *Adv. Meteorol. Sci. Technol.* **2017**, *7*, 128–133+148. (In Chinese)
54. Merrill, R.T. *An Experiment in Statistical Prediction of Tropical Cyclone Intensity Change*; US Department of Commerce, National Oceanic and Atmospheric Administration, National Weather Service, National Hurricane Center: Miami, FL, USA, 1987.
55. DeMaria, M.; Kaplan, J. Sea Surface Temperature and the Maximum Intensity of Atlantic Tropical Cyclones. *J. Clim.* **1994**, *7*, 1324–1334. [CrossRef]
56. Whitney, L.D.; Hobgood, J.S. The Relationship between Sea Surface Temperatures and Maximum Intensities of Tropical Cyclones in the Eastern North Pacific Ocean. *J. Clim.* **1997**, *10*, 2921–2930. [CrossRef]
57. Fitzpatrick, P.J. Understanding and forecasting tropical cyclone intensity change with the Typhoon Intensity Prediction Scheme (TIPS). *Weather Forecast.* **1997**, *12*, 826–846. [CrossRef]
58. Knaff, J.A.; Sampson, C.R.; DeMaria, M. An operational statistical typhoon intensity prediction scheme for the western North Pacific. *Weather Forecast.* **2005**, *20*, 688–699. [CrossRef]
59. Minola, L.; Zhang, F.; Azorín-Molina, C.; Safaei Pirooz, A.A.; Flay, R.G.J.; Hersbach, H.; Chen, D. Near-surface mean and gust wind speeds in ERA5 across Sweden: Towards an improved gust parametrization. *Clim. Dyn.* **2020**, *55*, 887–907. [CrossRef]